Lattice perfection and growth history of doubly-terminated natural alpha quartz crystals

A. R. LANG

H. H. Wills Physics Laboratory, University of Bristol, Tyndall Avenue, Bristol BS8 1TL, UK

A. P. W. MAKEPEACE

Department of Physiology, School of Medicine, University of Bristol, Bristol BS8 1TD, UK

AND

M. MOORE

Department of Physics, Royal Holloway, University of London, Egham, Surrey TW20 0EX, UK

Abstract

Synchrotron X-ray topography was the principal perfection-assessment method employed. X-ray wavelengths were chosen that gave optimum penetration and diffraction contrast characteristics for the size of crystals examined. Two colourless transparent specimens were selected for comprehensive study. Both were of simple habit consisting of the prism $\{10\bar{1}0\}$ terminated at each end by major and minor rhombohedral facets only. The larger specimen, volume ≈ 250 mm^3, contained a moderately high but non-uniformly distributed dislocation population, totalling $\approx 10^3$, all emanating from a roughly centrally located small nuclear volume. One apical region was dislocation-free. Optical microscopic observations including Nomarski interference contrast of features on one major rhombohedral facet in this region are described. The smaller specimen, volume ≈ 30 mm^3, was remarkable for its low dislocation content, ≈ 20 in total, all radiating from a central point. Enhancement of dislocation image visibility relative to diffraction contrast images of severe surface damage on this crystal was demonstrated using higher-order X-ray reflections. Neither of the specimens studied in detail contained twinning or evident diffraction contrast from impurity zoning. Their lack of a microscopically visible or X-ray topographically detectable nucleating body favours a homogenous nucleation origin of these crystals.

KEYWORDS: quartz, X-ray topography, dislocations, growth history

Introduction

SINGLE crystals of natural alpha quartz, as commonly encountered, take the shape of 'fingers', prisms gently tapering towards a terminating cap formed dominantly by the major, *r*, $\{10\bar{1}1\}$, and minor, *z* $\{1\bar{1}01\}$ rhombohedral faces. The finger base is the surface of fracture by which the specimen was detached from the cluster in which it grew up, the cluster substrate being typically the wall of a fissure or geode. It follows that with such specimens the earliest stages of growth, including the location and nature of the crystal nucleus, are inaccessible for study. Doubly-terminated crystals of alpha quartz are much rarer though they may be locally abundant, as in Herkimer County, New York State. A doubly-terminated habit is indeed expected in unconstrained quartz crystal growth, since the $\pm c$ directions are crystallographically equivalent. Doubly-terminated specimens would ideally appear as depicted in Figs. 7 and 8 of Frondel (1962), showing, for example, equal development of $(10\bar{1}1)$ and its inverse, $(\bar{1}01\bar{1})$. In a doubly-terminated quartz crystal, in contrast to a quartz 'finger', the whole growth history is encapsulated within its bounding surfaces, and so is in principle accessible for investigation.

The study of doubly-terminated quartz specimens here reported was directed principally towards probing the state of their long-range

Mineralogical Magazine, March 1994, Vol. 58, pp. 87–95

lattice perfection, to which end the non-destructive X-ray topographic technique was applied. (For descriptions of this method see Tanner, 1976, and Lang, 1978, 1992). Questions of interest included the following. Had the crystals grown out symmetrically from a single central nucleus? What is their lattice dislocation content? Where within the crystals were dislocations generated? Does high lattice perfection accompany the high optical perfection that some specimens exhibit? Can surface microtopographic features be correlated with dislocation outcrops? The experiments were directly revealing on the first three questions, and yielded some information bearing on the last two.

Experimental method

Methods of assessing the quality of quartz crystals by optical inspection and by studies of etch phenomena are well described by Heising (1946). Natural quartz figured early among crystal species to which the non-destructive X-ray topographic technique was applied (Lang 1959). Features that generate X-ray diffraction contrast, such as lattice dislocations, strain-producing inclusions, and local variations in lattice parameter, are of widespread occurrence in crystals; and the form their diffraction-contrast images take is largely independent of crystal species. It follows that X-ray topographs can generally provide an identification of the type as well as the concentration of lattice defects within the crystals. In the present context it is relevant to recall some X-ray topographic identifications of particular lattice defects in natural quartz. Heading the list are individual dislocations (Lang, 1959). Lattice-parallel twinning of Brazil and Dauphiné types can be detected and distinguished (Lang, 1965, 1967). Diffraction contrast generated at growth sector boundaries that results from growth-sector-dependent differences in quartz lattice parameters, and contrast arising from impurity zoning, have also been described (Lang, 1967).

The X-ray topographic experiments described below used continuous wavelength ('white' radiation) synchrotron X-rays. They were performed on Station 7.6 at the Synchrotron Radiation Source (SRS), SERC Daresbury Laboratory. Characteristics of white-radiation synchrotron X-ray topographic techniques are described in Lang (1992) and in reviews, e.g. Tanner and Bowen (1992). The high beam intensity and the freedom to select the optimum wavelength for the particular thickness of specimen under examination were the particular advantages offered by synchrotron radiation for the present experiments. Transmission X-ray topographs were recorded. Since the thickness of crystal to be passed through by the beam varied from a minimum at the apices to a maximum when traversing the prismatic cross-section, X-rays of wavelength sufficiently short so as not to be excessively absorbed in the thickest parts were needed. In one specimen this required X-rays of wavelength not greater than 0.5 Å, which is shorter than that of characteristic radiations available from conventional crystallographic X-ray tubes, the shortest being Ag-$K\alpha$ radiation, $\lambda = 0.56$ Å. However, white radiation transmission topographs of relatively thick crystals taken with short wavelengths tend to have a high background density, mainly attributable to air-scattering of longer wavelengths contained in the beam. Heavy filtration of the beam by aluminium sheets was employed with good effect to reduce this background. It provided low backgrounds, optical density <0.1, when the mean topograph image density was ≈ 1.0 (with locally much higher values in regions of high dislocation density or high diffraction contrast due to abrasion damage on the specimens). The great intensity of the synchrotron source ensured that the increase in exposure time required with heavy beam filtration involved but an insignificant reduction in experimental throughput per hour. All important X-ray topographs were recorded on Ilford L4 nuclear emulsion plates. The X-ray source dimensions, diffraction geometry and other factors determined the resolution of the topograph images. This was roughly 1–2 μm in the direction of the diffraction vector, which was the direction normal to the horizontal electron orbit plane of the synchrotron, and about 3 μm in the direction normal to the diffraction vector, i.e. in the horizontal plane.

Selection and setting of specimens

It was deemed scientifically more profitable to employ the available synchrotron beam time for detailed study of a few specimens rather than cursory examination of many. Specimen selection was made from the collections in the Geology Departments of Royal Holloway, University of London, and of Bristol University. X-ray topographic experiments were performed on three specimens, two of gem, or near-gem quality, and the third a representative of those with good morphology but lacking optical transparency. All specimens had simple morphology, exhibiting only forms *r*, *z* and prism *m*, $\{10\bar{1}0\}$. Since faces, *s*, $\{11\bar{2}1\}$, and *x*, $\{51\bar{6}1\}$, were absent, the morphological hand was not evident, but it was not relevant in the present study. All specimens

showed *m* faces unusually smooth compared with the striated surfaces commonly observed on quartz 'fingers'. Of the two transparent and perfectly colourless crystals, the larger (hereafter called Specimen 1) did contain a few visible flaws, including a couple of cracks. The smaller (Specimen 2) was quite flawless; its source was identified as New York State. Specimen 3 was uniformly milky; its X-ray topographs did not exhibit features directly interpretable in terms of a configuration of dislocations, and it will not be considered further. Specimen dimensions were as follows. Specimen 1: apex-to-apex 10.7 mm; diameters between *m* faces differed little, average value 6.5 mm. Specimen 2: apex-to-apex 5.5 mm; diameters between *m* faces, 2.6, 2.8 and 3.0 mm.

In setting up specimens for X-ray topography, standard-size X-ray crystallographic goniometer heads were adapted. To facilitate rapid switching between Bragg reflections from the several *r* and *z* planes that were used, each crystal was mounted on a small rotatable spindle parallel to its *c*-axis. The spindles were carried by angled brackets attached to the standard detachable specimen-mounting platforms that fit on the goniometer heads. The bend of the brackets was such as to make the angle between the axis of the rotatable spindle and the normal rotation axis of the whole goniometer head about its base to be as near as possible to 38°13′, the angle that *r* and *z* planes make with the *c*-axis. Each specimen had one of its apices seated in the cup formed by the bore of a nylon nut, to which it was attached by Araldite. The nylon nut was locked to one end of the rotatable spindle. Both nylon and Araldite being X-ray transparent compared with quartz, they produced no unwanted shadow, nor significant additional scattering on the topograph images. The attachment of crystals to the nylon nuts was in fact effected with two stages of Araldite use, the first involving moulding a stable mechanical support and the second involving the controlled orientational setting of the specimen. Before transportation to the SRS each specimen was set for its first rhombohedral reflection. At the SRS, switching to the next desired reflecting plane was achieved by rotating the crystal-carrying spindle by an integral number of 60° steps, plus such minor adjustment of one of the arcs of the goniometer head as was needed to bring the diffraction vector accurately into the plane normal to the main goniometer rotation axis, i.e. the ω-axis by which the Bragg angle was set. This adjustment, together with the establishment of zero angle on the Bragg-angle rotation scale, were performed on the X-ray topography camera with the aid of a laser beam accurately aligned anti-parallel to the incident synchrotron X-ray beam. The better crystal faces gave reflected laser beam signals sharp enough to allow specimen orientation settings on the camera to be made within a few milliradians, and with no more than a few minutes' efforts.

Observations

Specimen 1. For the X-ray topographic survey of this crystal all the major rhombohedral faces were used as Bragg planes. These topographs provided six different projections of the crystal volume. The pair of projections formed by reflections from a given plane and its inverse constitute a stereopair corresponding to a visual convergence angle $2\theta_B$, where θ_B is the Bragg angle, 4.3° in these experiments. Figure 1 *a* shows one member of such a pair. Stereopair images on the original nuclear emulsion plates could be studied using twin low-power microscopes. This greatly assisted in spatially locating sources of diffraction contrast, and in particular in distinguishing between internal sources and those correspond-ing to natural abrasion damage on the surfaces, which was abundant. The dislocation content of this specimen is moderately high, but non-uniformly distributed. The total dislocation number is estimated to be of order 10^3. It appears that all dislocations were generated in a nuclear volume small compared with the overall crystal size; from this small volume they radiate outwards in many directions. It follows that dislocation concentration in the crystal (integrated line length per unit crystal volume) decreases outwards from the nucleus. Only in outer regions of the crystal can individual dislocation images be resolved, appearing as fine lines in Fig. 1*a*. However, in the upper apical region in Fig. 1*a*, which is capped by rhombohedral faces to which positive *l* index has been assigned, a volume of ≈ 10 mm^3 dislocation-free is found. No Dauphiné or Brazil twinning is evident. The additional diffraction contrast due to strains associated with burring along the crystal edges causes these edges to be imaged on the topographs.

The diagram Fig. 1*b* identifies certain features seen on the topograph image Fig 1*a*. For simplicity the outline of the crystal is drawn as if viewed parallel to $[\bar{1}2\bar{1}0]$, whereas the topograph image corresponds to a projected view of the crystal along the diffracted beam direction, which makes $\theta_B = 4.3°$ with $[\bar{1}2\bar{1}0]$. (This geometrical discrepancy between Figs. 1*a* and *b* is unimportant; diffraction contrast from the damaged near and far edges of the face $(\bar{1}010)$ is so strong that images of these two edges are not seen

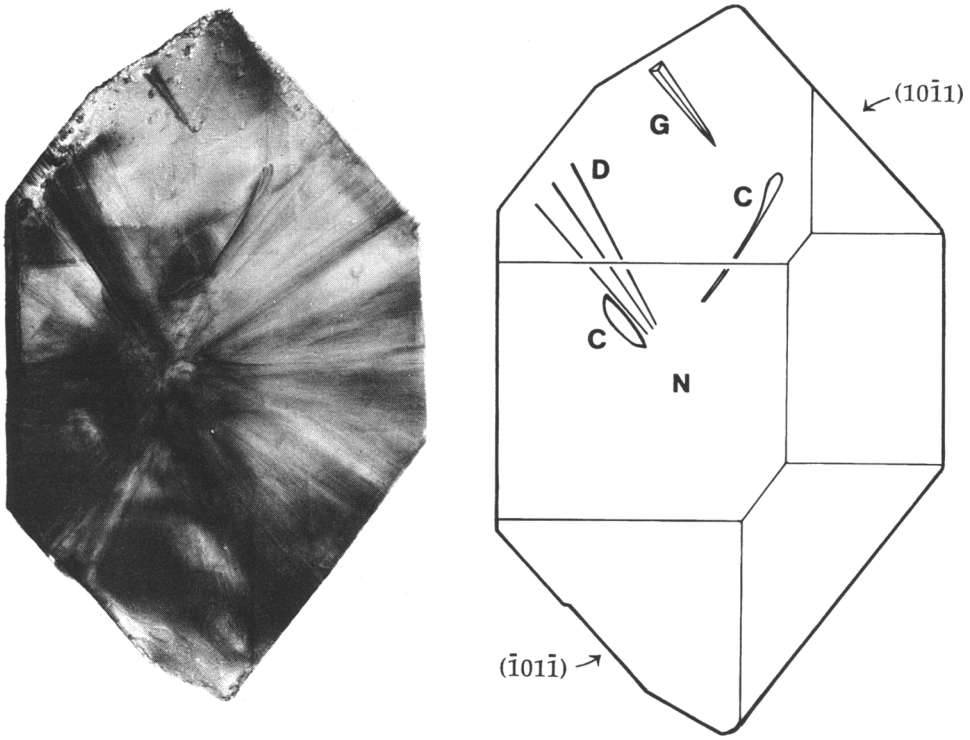

FIG. 1. (*a*) X-ray projection topograph of Specimen 1, reflection $\bar{1}01\bar{1}$, diffraction vector points to lower left, synchrotron radiation wavelength 0.5 Å, filtered by 1.4 mm aluminium, Bragg angle $\theta_B = 4.3°$. (*b*) Key to X-ray topograph Fig. 1 (*a*). Projection simplified by showing crystal outline as viewed parallel to prism faces $\pm(10\bar{1}0)$. Diameter between faces $\pm(10\bar{1}0)$ is 6.5 mm. Fine continuous lines indicate loci on Fig 1 *a* of images of crystal edges on the X-ray exit surface of the crystal. Lettered features described in text.

separated on the topograph, but merged together as one thick black band.) In Fig. 1*a* the crystal nucleus N appears close to the geometric centre of the crystal. However, combination with measurements on other projections shows that N lies about 2 mm off the centroid of the prism cross-section, being displaced towards $(0\bar{1}10)$. The features labelled C identify the topograph images of the two visible cracks that have been mentioned above. The dislocations D are picked out for notice as being the largest bundle appearing on facets of the upper cap. In the vicinity of their outcrops, which is on $(\bar{1}101)$, prominent growth hillocks are seen.

The feature G, which produces quite strong contrast in Fig 1*a*, lies on the $(0\bar{1}11)$ face, and is also shown in Fig. 2. The latter figure correctly depicts the relative development of *r* and *z* faces on the upward-pointing cap in Fig. 1*a* and *b*. Face $(0\bar{1}11)$ attracted attention since it gave a sharper laser beam reflection than any other faces illuminated. However, when the laser beam (which was about 1 mm in diameter) impinged on one area close to the edge between this face and $(0\bar{1}10)$ the back-reflected light formed roughly a circle when projected on a screen. This indicated reflection from a surface roughly conical, presumably a growth hillock. From the diameter of the circle measured on a screen 1 m distant from the crystal, the mean slope of the vicinal surfaces surrounding the hillock was estimated to be about 1 milliradian. Microscopic examination of the $(0\bar{1}11)$ face did in fact confirm its unusual flatness, and that it was entirely covered by growth steps emanating from a single centre, located close to the edge with $(0\bar{1}10)$, near P in Fig. 2. In this region of the crystal, dislocations were not sufficiently sparse to make possible the identification of a particular individual outcrop with this growth centre.

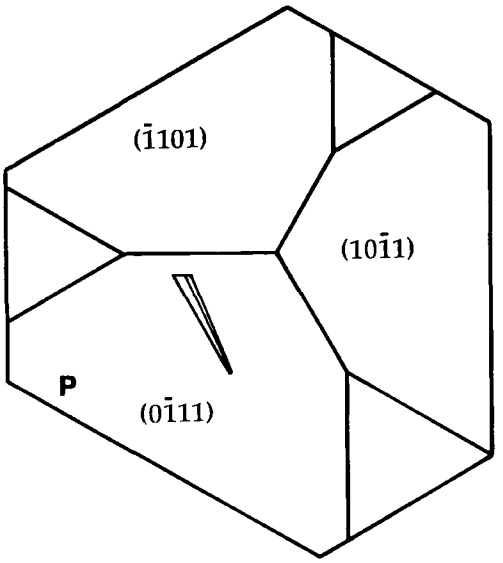

FIG. 2. Drawing of upper cap of Specimen 1 viewed parallel to *c*. (Measurements by projection microscope.) Major rhombohedral facets indexed. Location of dominant growth centre on (0$\bar{1}$11) indicated by P.

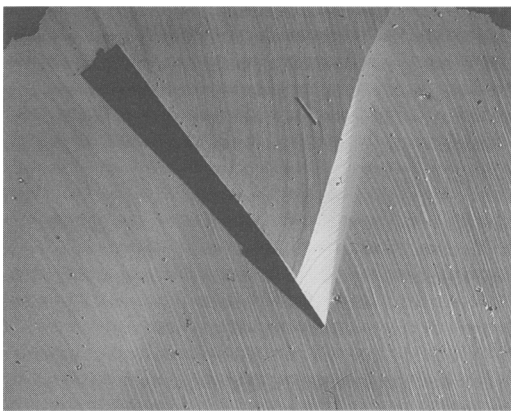

FIG. 3 Nomarski interference contrast micrograph of near-apical region on face (0$\bar{1}$11) of Specimen 1. Edges with ($\bar{1}$101) and (10$\bar{1}$1) appear in top left and top right corners of images, respectively; projection of [0001] points vertically upwards. Field width 2.67 mm. Depressed feature G shows solid black. The Nomarski contrast simulates illumination from the upper left. Hence the sloping wavefront of steps sweeping around the lower end of G, and which slopes towards the upper left, appears bright.

Returning to object G, this feature is believed to be of importance. Thought at first to be a severe scratch or gouge on the basis of its X-ray topographic images, optical microscopic examination showed it to be sharply linearly bounded, apparently the imprint of an edge of a faceted body. The inward-sloping surfaces of the imprint appeared rough, so the re-entrant angle could not be measured. Nomarski interference microscopy of the (0$\bar{1}$11) face was informative. It picked out growth layers spreading over the face from P, and revealed that G had behaved as an obstacle to their spreading. The Nomarski micrograph Fig. 3 shows that layers have swept round the lower end of G and have piled up to form a 'wave', a sloping surface with a sharply defined foot. This sloping surface appears bright in Fig. 3. Where it meets G, the measured height difference between foot and upper edge of the 'wave' is about 1 μm, measured relative to the mean (0$\bar{1}$11) surface; and the distance from foot to upper edge is 200 μm.

Specimen 2. Stereopairs of reflections from some major and minor rhombohedral planes were used in the X-ray topographic survey of this crystal, and a comparison was made between first-order and second-order reflections. The noteworthy characteristic of Specimen 2 was its low dislocation content: the whole specimen contained probably not more than 20 dislocations. Equally remarkable, unfortunately, was the severity of surface damage. The diffraction contrast from deformations associated with this mechanical damage blanketed the topograph images, rendering difficult the detection of individual dislocations. For example, in the pair of topographs formed by the major rhombohedral reflections indexed $\bar{1}101$ and $1\bar{1}0\bar{1}$ (not shown here) close microscopic examination was needed to discover dislocation images amongst the population of flecks and streaks due to surface damage. However, the dependence of dislocation image profile upon order of reflection and magnitude of X-ray structure factor could be exploited to render their images more visible relative to images of surface indents and scratches, as is demonstrated in topographs selected for reproduction here, and discussed later. Specimen 2 was free from twinning.

The habit of Specimen 2 is less regular than that of Specimen 1. In particular, two of its prism faces [those indexed ($\bar{1}$010) and (0$\bar{1}$10)] were extended considerably longer parallel to the *c*-axis than the other prism faces. The atypical relative development of *r* and *z* rhombohedral

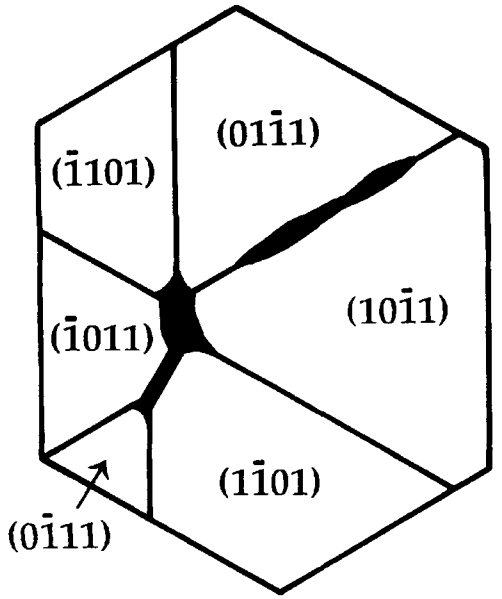

FIG. 4 Relative development of rhombohedral facets on the cap of Specimen 2 that points upwards in Figs. 5 and 6. Particularly heavy damage that has destroyed crystal edges is indicated by solid black. Diameters between prism faces $\pm(10\bar{1}0)$, $\pm(0\bar{1}10)$ and $\pm(\bar{1}100)$ are 2.6, 2.8 and 3.0 mm respectively.

faces on the cap whose projection parallel to *c* is drawn in Fig. 4 can be explained by this unequal development of prism faces. In Fig. 4 the indexing of facets as major or minor rhombohedral was based on relative intensities of X-ray reflections seen in the Laue-type patterns that the continuous spectrum of synchrotron radiation produced. An X-ray topograph of one of the major rhombohedral reflections, $\bar{1}01\bar{1}$, is shown in Fig. 5*a*. In this pattern a few dislocation images can be picked out. (When examined together with the stereotwin topograph, reflection $10\bar{1}1$, detection is somewhat easier.) All face scratches and edge burrs that can be seen on the specimen surface under low-power microscopic examination have their matching diffraction contrast images on this and other X-ray topographs. The drawing Fig. 5*b* distinguishes between images of burred edges that lie on the X-ray entrance surface or exit surface of the specimen, and it identifies a few dislocation images that fan outwards from a nucleus of unresolved small dimension. (This drawing only approximates to true geometry. For simplicity it shows the crystal outline projected parallel to $[\bar{1}2\bar{1}0]$, but the projections of the crystal edges running parallel to the *c*-axis, and projections of dislocation images, are drawn to match their positions on the topograph Fig. 5*a*.)

The X-ray topograph seen in Fig. 5*c*, taken with the second order of a minor rhombohedral reflection, but with the same wavelength as used for Fig. 5*a*, presents a very different type of image. The changed diffraction conditions cause loss of resolution of most individual scratches and indents, and their images are largely merged together. Images of dislocations are also much broadened. Since the dislocation images run as straight lines through a variable background that has smaller density gradients than in the first-order reflections, their detectability is considerably improved.

Another illustration of dislocation visibility enhancement is provided by Fig. 6*a* and *b*, the first and second-order reflections from a minor rhombohedral plane. The first order lacks the resolution of small-scale abrasion damage that is given by fig. 5*a*; note, for example, the more diffuse images of crystal edges that appear in Fig 6*a*. On the other hand, the latter figure shows better visibility of dislocation images than Fig. 5*a*. In the second-order reflection, Fig. 6*b*, the dislocation lines radiating from the central nucleus stand out clearly as they do in Fig. 5*c*. Running downwards from the upper apex of the crystal projection seen in Fig. 6*a* and *b* there is a band of very strong contrast. This corresponds to the very badly damaged edge between $(01\bar{1}1)$ and $(10\bar{1}1)$ indicated by black in Fig. 4. On the other hand, an arc of higher density running roughly vertically close to the lower segment of the nearly edge-on projection of face $(\bar{1}100)$ that forms the left-hand vertical edge of the images in Fig. 6*a* and *b* does not correlate with a visible surface feature, and appears to be caused by an internal defect of undetermined nature laying close to the $(\bar{1}010)$ surface.

Discussion

Progress made towards answering the questions posed in the Introduction is summarized under the headings following. Though derived from so small a number of specimens, it is believed that the findings listed do serve as a fair foundation for description of the lattice perfection in doubly-terminated natural quartz.

Dislocation content. As the X-ray topographs of Specimen 2 have demonstrated, doubly-terminated crystals can grow nearly dislocation-free. In both Specimens 1 and 2 it was found that all the dislocations in the crystal radiate outwards from a central (or near-central) nuclear volume, which is

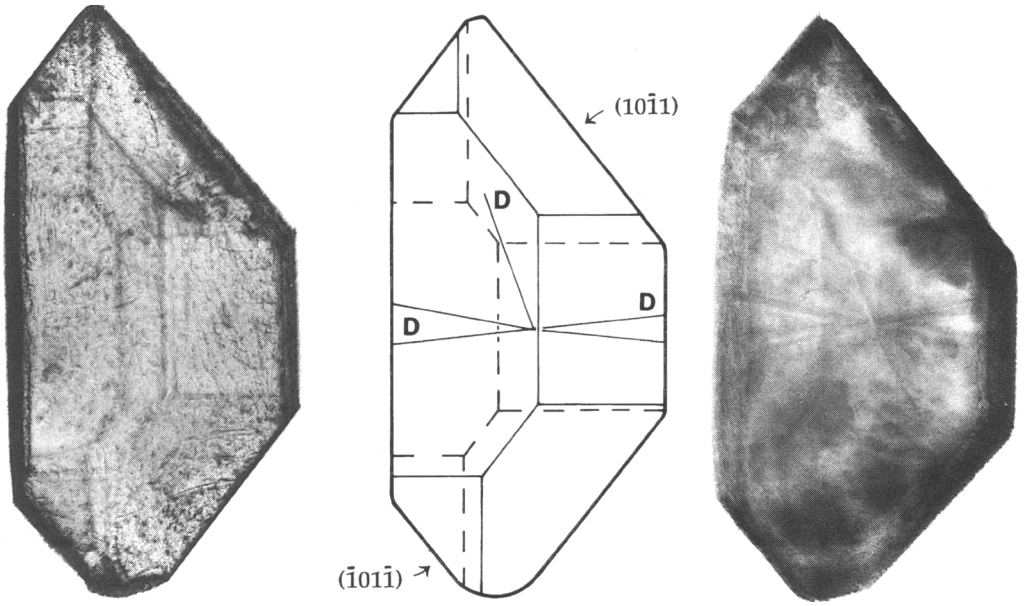

FIG. 5. (*a*) X-ray projection topograph of Specimen 2. Reflection $\bar{1}01\bar{1}$, diffraction vector points to lower left. Bragg angle $\theta_B = 5.5°$. This and other X-ray topographs of Specimen 2 taken with synchrotron radiation wavelength 0.64 Å, filtered by 0.9 mm aluminium. (*b*) Key to X-ray topograph Fig. 5 *a*. Outline of crystal shown as viewed parallel to [$\bar{1}2\bar{1}0$]. Images of crystal edges on X-ray exit surface (continuous lines), on X-ray entrance surface (interrupted lines), and dislocation images D, sketched roughly as they appear in Fig. 5 *a*. (*c*) X-ray projection topograph of Specimen 2. Reflection $20\bar{2}\bar{2}$, diffraction vector points to lower right. $\theta_B = 11°$.

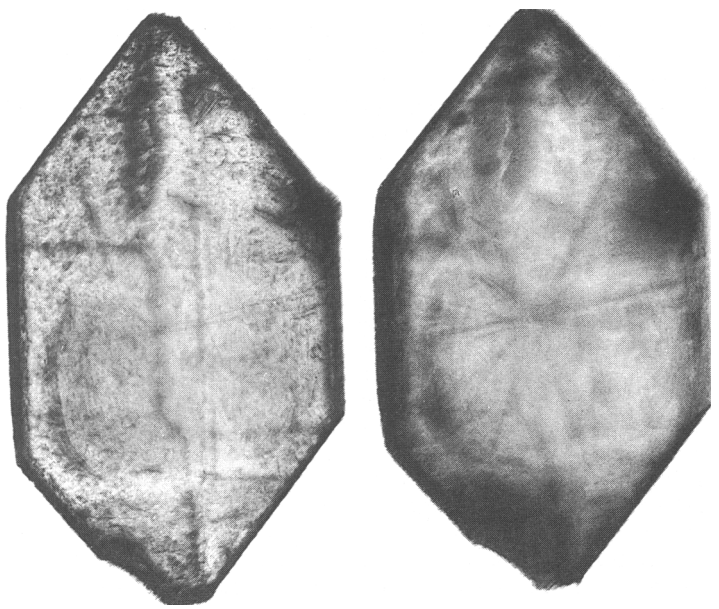

FIG. 6 X-ray projection topographs of Specimen 2. (*a*) Reflection $\bar{1}10\bar{1}$, diffraction vector points to lower left. (*b*) Reflection $\bar{2}20\bar{2}$.

TABLE 1. Calculated X-ray extinction distances and 'perfect-crystal' angular reflection ranges for major and minor rhombohedral reflections of alpha quartz. X-ray wavelength 0.64 Å.

Reflection	F	ξ/μm	W/arc seconds
$10\bar{1}1$, *r*	39.3	50	2.76
$20\bar{2}2$	18.1	107	0.65
$10\bar{1}\bar{1}$, *z*	25.7	76	1.81
$20\bar{2}\bar{2}$	8.9	217	0.32

of microscopic dimensions in the case of Specimen 2. With the freedom from overlapping dislocation images that the low dislocation population in Specimen 2 exhibits, standard X-ray topographic techniques should be applicable to determine the Burgers vectors of individual dislocations. In practice this is impossible because the obscuring of dislocation images by contrast from surface damage would prevent proper assessment of the dependence of dislocation image visibility upon orientation of diffraction vector. (The obscuring could have been reduced or eliminated by the impermissible operation of deeply etching the surfaces.)

Dislocation contrast. The notable difference between topographs taken with first and second-order reflections merits brief explanation. A simple model for estimating the width of the diffraction contrast image of an individual dislocation in a matrix of perfect crystal (Lang 1959, 1978; Tanner 1976) assumes that significant rise in diffracted intensity begins at such distance, *r*, from the dislocation core that the local lattice tilt due to the dislocation strain-field has reached a magnitude about equal to the angular range of reflection, *W*, of X-rays by the perfect crystal matrix. In dislocation strain-fields the lattice tilt falls off as $1/r$, so when *W* is small, the apparent width of the dislocation image, $2r$, is large. Under the diffraction conditions applying in the present experiments, *W* can be taken as the full width at half maximum intensity of the reflection transmitted by a non-absorbing perfect crystal, and is simply $W = 2d/\xi_g$, where *d* is the interplanar spacing and ξ_g is the X-ray extinction distance for the reflection concerned. With the polarized synchrotron radiation used, the reciprocal of the extinction distance is given by $\xi_g^{-1} = r_e F\lambda/(\pi V \cos\theta_B)$, where r_e is the classical electron radius (2.82×10^{-15} m), λ is the X-ray wavelength, *V* is the volume of the unit cell (113 Å^3 for alpha quartz) and F is the X-ray structure factor. Inserting the wavelength used in the experiments on Specimen 2 (0.64 Å), and calculated F values given by Zachariasen and Plettinger (1965) (bearing in mind that those authors indexed *r* as $(10.\bar{1})$ and *z* as (10.1)) the values of ξ_g (in μm) and *W* (in seconds of arc) for the quartz reflections used are listed in Table 1.

It is seen that the magnitude of *W* for the reflection shown in Fig. 5*c* and for the equivalent reflection in Fig. 6*b* is but a small fraction of *W* for the reflection in Fig. 5*a*, and this accounts for the much wider dislocation images in the former topographs. Since other defects, such as surface scratches, produce lattice tilts falling off roughly inversely as distance from the strain centre, the general blurring of their images accompanying decrease in *W* is also understandable.

Long-range lattice perfection. In the presence of so much diffracted intensity from surface damage it is impossible to make direct use of diffraction contrast characteristics of the topographs to compare the long-range lattice perfection in these quartz crystals with that of, say, a perfect silicon specimen. Such comparison could be made semi-quantitatively by comparing the intensity of dislocation images relative to background diffracted intensity, using surface-damage-free specimens of both crystal species. In Specimens 1 and 2 the detectability of individual dislocation images does at least show that lattice periodicity is sufficiently good to maintain coherent X-ray reflection over distances of order ξ_g. It deserves noting that in topographs of Specimen 1 and 2 no diffraction-contrast evidence of impurity zoning is seen, though sensitive testing for such would require X-ray topography of surface-damage-free slices cut from the specimens.

Surface microtopography. Specimen 1 contained too many dislocations to be a good subject on which to try and correlate dislocation outcrops with summits of growth hillocks, but one general correlation of this sort has been mentioned above. Specimen 2 had a more suitable dislocation content for such studies, but its surfaces were quite unsuitable for this purpose. All were rough on a fine scale. All rhombohedral faces had much of their areas covered with a dense population of overlapping low-elevation pyramids, suggesting that in the final stages of growth there existed a high density of simultaneously operating growth centres on those surfaces.

Growth history. That the point or small volume in the crystals from which dislocations radiate in *all* directions defines the nucleus from which growth proceeded is a geometric certainty. Absence of microscopically visible or X-ray topographically detectable nucleating bodies favours (but does not prove) a homogeneous

nucleation origin of these specimens. In Specimen 1 the dislocations appear all to have been generated within a nuclear volume about 0.3 mm in diameter; perhaps such generation accompanied an initial stage of rapid growth. The doubly-terminated habit necessarily indicates growth unconstrained by other substantial solid bodies, and implies growth in a supporting medium capable of flow: a silica gel is likely. Freedom from dislocation generation at any point other than the central nucleus points to growth in a medium free from small bodies likely to suffer incorporation in the growing quartz crystal, and which act thereby as a source of dislocations resulting from lattice closure errors in the engulfing quartz crystal lattice. However, the finding of feature G on Specimen 1, interpreted as a relic of contact with another sizeable faceted body, shows that in the case of this specimen growth did not take place remote from other crystals. The morphology of the faceted body that left imprint G cannot be established. The presence of local lattice damage at G, revealed by the diffraction contrast, suggests a measure of 'welding' or intergrowth with the body that has been removed from G. Such would be understandable if the body had been another quartz crystal. Identity of the two structures might be expected to enhance the probability that during the time the crystals were joined together the re-entrant angles between them would have acted as sources of growth layers. In fact Fig. 4 shows a different effect, G having behaved as an obstacle to growth layers spreading from P. Perhaps the two crystals became parted before the final stage of growth on the face of Specimen 1.

Acknowledgements

The authors thank the Director and Staff of the SERC Daresbury Laboratory for the provision of experimental facilities. Thanks are also due to the Departments of Geology at the University of Bristol and at Royal Holloway, University of London, for loan of specimens. Financial support from the UK Science and Engineering Research Council is gratefully acknowledged.

References

Frondel, C. (1962) *Dana's System of Mineralogy*. Vol. **3**, *Silica Minerals*. Wiley, New York.

Heising, R. A. (1946) *Quartz Crystals for Electrical Circuits*. van Nostrand, New York.

Lang, A. R. (1959) Studies of individual dislocations in crystals by X-ray diffraction microradiography. *J. Appl. Phys.*, **30**, 1748–55.

Lang, A. R. (1965) Mapping Dauphiné and Brazil twins in quartz. *Appl. Phys. Lett.*, **7**, 214–6.

Lang, A. R. (1967) Fault surfaces in alpha quartz: their analysis by X-ray diffraction contrast and their bearing on growth history and impurity distribution. *J. Phys. Chem. Solids, Supplement No.1*, 833–8.

Lang, A. R. (1978) Techniques and interpretation in X-ray topography. In *Diffraction and Imaging Techniques in Material Science*, 2nd edn. (S. Amelinckx, R. Gevers and J. van Landuyt, eds.) North Holland, Amsterdam, pp 623–714.

Lang, A. R. (1992) X-ray topography. In *International Tables for Crystallography, Vol.C* (A. J. C. Wilson, ed.) Kluwer Academic Publishers, Dordrecht. Chap 2.7, pp113–36.

Tanner, B. K. (1976) *X-ray Diffraction Topography*. Pergamon, Oxford.

Tanner, B. K. and Bowen, D. K. (1992) Synchrotron X-radiation topography. *Materials Science Reports*, **8**, 369–407.

Zachariasen, W. H. and Plettinger, H. A. (1965) Extinction in quartz. *Acta Crystallogr.*, **18**, 710–4.

[*Manuscript received 30 April 1993: revised 2 June 1993*]